


 Cite this: *Lab Chip*, 2019, 19, 3045

Acoustofluidic stick-and-play micropump built on foil for single-cell trapping†

 Yang Lin,^a Yuan Gao,^a Mengren Wu,^a Ran Zhou,^b Daayun Chung,^c Gabriela Caraveo^c and Jie Xu^{*,a}

The majority of microfluidic devices nowadays are built on rigid or bulky substrates such as glass slides and polydimethylsiloxane (PDMS) slabs, and heavily rely on external equipment such as syringe pumps. Although a variety of micropumps have been developed in the past, few of them are suitable for flexible microfluidics or lab-on-a-foil systems. In this paper, stick-and-play acoustic micropump is built on thin and flexible plastic film by printing microstructures termed defended oscillating membrane equipped structures (DOMES) using two-photon polymerization. Specifically, this new micropump induces rectified flow upon the actuation of acoustic waves, and the flow patterns agree with simulation results very well. More importantly, the developed micropump has the capabilities to generate adjustable flow rates as high as 420 nL min⁻¹, and does not suffer from problems such as bubble instability, gas dissolution, and undesired bubble-trapping that commonly occur in other forms of acoustic micropumps. Since the micropump works in stick-and-play mode, it is reusable after cleaning thanks to the easy separation of covers and substrates. Lastly, the developed micropump is applied for creating a self-pumped single-cell trapping device. The excellent trapping capability of the integrated device proves its potential for long-term studies of biological behaviors of individual cells for biomedical applications.

 Received 22nd May 2019,
Accepted 5th August 2019

DOI: 10.1039/c9lc00484j

rsc.li/loc

1. Introduction

Ever since Manz and co-workers announced the birth of micro total analysis systems (μ TAS) nearly three decades ago,¹ microfluidics or the so-called lab-on-a-chip has undergone rapid growth and spawned a plethora of applications in different fields such as biology,² chemistry,³ pharmacology,⁴ environmental monitoring,⁵ and others.^{6,7} Unfortunately, the majority of these applications heavily rely on off-chip equipment (e.g., syringe pumps) to maintain required conditions (e.g., constant flow rates).⁸ Therefore, in most cases, microfluidics nowadays remains an exclusive platform in research laboratories, and the dependence of external devices has become a roadblock for commercialization. Nevertheless, on-chip functions such as pumping,⁹ mixing,¹⁰ filtering¹¹ and analysis¹² have been widely explored, towards fully automated microfluidic systems over the past years. Among them, pumping is a fundamental function that bridges the micro

and macro environments, and enables precise manipulation of fluids through systems for different purposes, including drug delivery,¹³ cell separation,¹⁴ biomedical analysis,¹⁵ and so forth.^{16–19} Based on different driving mechanisms, micropumps in microfluidic systems can be primarily categorized into two classes: mechanical and non-mechanical.¹⁷ The former one displaces fluids *via* moving mechanical parts (e.g., pumping diaphragms or check valves).^{20–22} Although these micropumps possess attractive pumping performances, sophisticated designs and complex fabrication processes are usually required.¹⁷ On the contrary, the alternative type transforms non-mechanical energy into kinetic momentum of fluids by means of magnetohydrodynamics,²³ electrohydrodynamics,²⁴ electroosmosis,²⁵ and other effects.^{26,27}

Unsurprisingly, acoustic energy has also been explored for creating micropumps.²⁸ For instance, micropumps based on surface acoustic wave (SAW) have been exploited and used for various applications over the past years.^{29,30} That said, most of these devices were built on rigid piezoelectric substrates (e.g., LiNbO₃) and usually required sophisticated vapor deposition for the fabrication of interdigital transducer (IDT).³¹ Therefore, bendable SAW devices built on thin and cheap substrates have become an alternative platform and pioneered several applications.^{32,33}

On the other hand, acoustic micropumps based on bulk acoustic waves (usually coupled with acoustic bubbles or

^a Department of Mechanical and Industrial Engineering, University of Illinois at Chicago, Chicago, USA. E-mail: jixu@uic.edu

^b Department of Mechanical and Civil Engineering, Purdue University Northwest, Hammond, USA

^c The Ken & Ruth Davee Department of Neurology, Feinberg School of Medicine, Northwestern University, Chicago, USA

† Electronic supplementary information (ESI) available. See DOI: 10.1039/c9lc00484j

sharp edges) have also emerged as promising tools owing to the ease of operation and programmable flow rates.^{8,9,26,34} Tovar and Lee have developed a micropump termed lateral cavity acoustic transducer (LCAT),⁸ which drives fluids using 20 pairs of air-bubbles trapped in angled lateral cavities. However, similar to free acoustic bubbles, these LCATs suffered from bubble instability and gas dissolution. For example, trapped bubbles can expand into the main microchannels or disappear due to diffusion or dissolution. As a result, pumping performance is challenging to be maintained for a long time. Apart from acoustic bubbles, solid sharp edges have also been investigated for creating micropumps by Huang and co-workers.⁹ They found the proposed micropumps were capable of tuning the flow rates across a wide range (nL min^{-1} to $\mu\text{L min}^{-1}$). Nonetheless, one limitation lay in this device was that the pumping performance was sensitive and subject to undesired bubble-trapping, which may occur at the corners between tilted cantilevers and side walls.

In addition, most of the acoustofluidic devices developed hitherto were placed on glass substrates, and in turn they were inflexible, brittle, and unsuitable for applications involving non-planar and/or flexible surfaces. Moreover, despite possessing irreversible bonding with high strengths obtained from plasma treatments, such bonding between polydimethylsiloxane (PDMS) and glass substrates in these devices made themselves impossible to be cleaned and reused in a simple way. Therefore, reversible bonding that allows stick-and-play has become an alternative for building microfluidic systems especially when it comes to applications where low bonding strength is sufficient.^{35,36}

In this paper, we report a robust stick-and-play micropump-on-the-foil with tunable flow rates at a resolution of nanoliter per minute. The device is based on pore-containing microstructures termed defended oscillating membrane equipped structures (DOMES), which is excited by acoustic actuation. We have recently shown that symmetric dome-shaped DOMES interact with acoustic energy and create mixing effects due to acoustic microstreaming (*i.e.*, a net time-averaged flow induced by harmonic perturbation of air-liquid interfaces trapped in the DOMES).³⁷ In present study, we explore a new type of DOMES with asymmetrical structures and report its ability to produce net flow for pumping biological samples in a lab-on-a-foil device. Compared to conventional counterparts, lab-on-a-foil devices are built on thin and flexible substrates,³⁸ thus bringing several advantages to practical usage. For instance, fabrication techniques such as roll-to-roll embossing can be adapted for commercial mass production. These devices are also considered as disposable consumables since little materials are required.³⁹ Moreover, biological reactions (*e.g.*, polymerase chain reaction) that are sensitive to temperature change are easier to achieve due to inherently small thickness of substrates.⁴⁰

In this study, we also apply the micropump-integrated lab-on-a-foil to perform single-cell trapping, which is an important first step that enables downstream single cell analysis. It is well accepted that bulk experiments that account for

collecting statistical data from a large number of cells are often not adequate for interpreting the individual differences between cells,^{41–43} and single-cell analysis overcomes this shortcoming and offers invaluable insights at single-cell level (*e.g.*, heterogeneity of stem cells). Thus single cell analysis has gained increasing attentions over the past years,^{44,45} along with numerous applications using microfluidics.⁴⁶ For example, on-chip flow cytometry has shown excellent capabilities of cellular manipulation and characterization in a high-throughput way (more than 50 000 cells per second).⁴⁷ Droplet-based single-cell screening also provides an alternative method to tackle single-cell analysis rapidly.^{48,49} Nevertheless, these methods lack temporal resolution that reflects the cellular changes over time. In such cases, their results may lead to misinterpreted conclusions. Given this concern, long-term observation or imaging could provide a solution to decipher correlated misunderstandings,⁵⁰ and this can be achieved using single-cell trapping methods that retain the cells at preset locations.⁵¹ In the past, a variety of approaches have been explored to do so, including encaging trapping,^{46,52} hydrodynamic trapping,⁴³ dielectrophoretic trapping,⁵³ optical tweezer trapping,⁵⁴ and others.⁵⁵ In this paper, simple 3D cell cages were adopted, and combined with DOMES-based micropumps for creating self-pumped lab-on-a-foil devices to carry out single-cell trapping on the foil.

2. Materials and methods

2.1 Overall fabrication process

The stick-and-play microfluidic device consists of two layers: the top PDMS layer and the bottom PET layer (Fig. 1a). Through holes (180 μm diameter) were pre-cut in the indium tin oxide (ITO)-coated PET films (127 μm in thickness, Sigma-Aldrich, St. Louis) using a milling machine (CNC Mini-Mill/3, Minitech Machinery Corp., Atlanta, GA). DOMES structures were created using two-photon polymerization (TPP), a three-dimensional (3D) printing technology with extremely high resolution.⁵⁶ The TPP system used here is a Nanoscribe system (Nanoscribe Photonic Professional GT, Nanoscribe GmbH, Germany). As shown in Fig. 1, thanks to the through hole in the PET substrate, the air-liquid interfaces formed in the pores of the DOMES structure is now open to the ambient air subject to atmospheric pressure. These air-liquid interfaces (or membranes) acted in a similar way to a bubble surface in an acoustic field, *i.e.*, oscillating upon acoustic actuation and creating microstreaming flow.

The fabrication process is briefly described as follows. The PET film with a through hole in it was first cleaned with acetone and isopropyl alcohol (IPA) rinse, followed by nitrogen blow-drying. Afterwards, a small amount of the photoresist (IP-S, Nanoscribe GmbH, Germany) was added onto the ITO-coated side of the film. This thin layer of ITO made the TPP system capable of finding the interface between the photoresist and the film.⁵⁷ Hence, floating microstructures created inside the resin can be avoided. During fabrication, an adaptive slicing (0.2–1.0 μm) and a hatching of 0.3 μm were

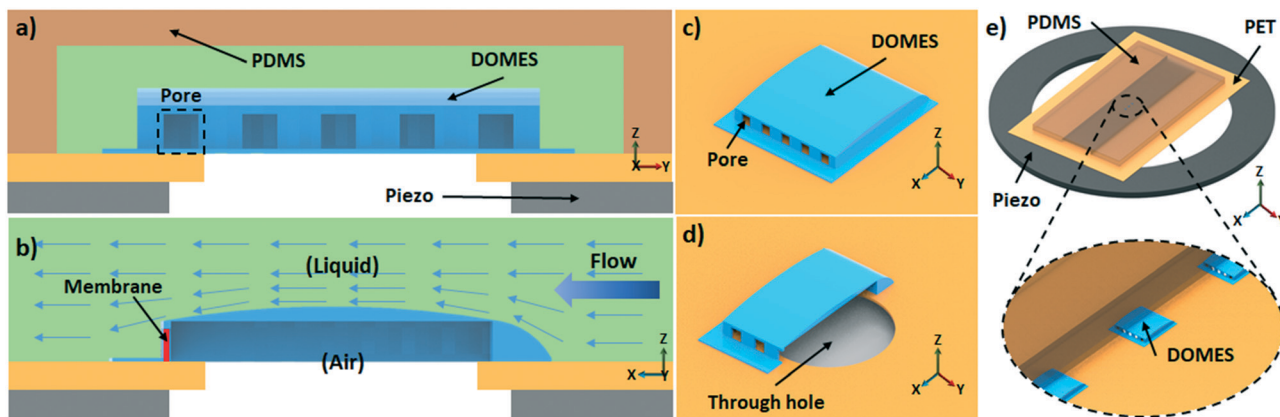


Fig. 1 Schematic illustration of the micropump based on DOMES. a) Cross section of the stick-and-play micropump on the foil. A PET film with printed DOMES was attached on a ring-shaped piezo using double-sided tape. Thereafter, the PDMS cover with microchannels was attached manually and carefully onto the PET substrate without further treatment; b) side view of micropump based on the DOMES created above a through hole in the PET film. The interfaces were kept facing ambient air across the holes in the PET film and the piezo; c) 3D model of the DOMES; d) 3D model of the half DOMES created above a through hole; e) schematic illustration of the final device attached to the piezo. Schemes only represent relative position of objects rather than actual size.

applied, upon which the total fabrication time for a DOMES was found to be approximately 5 minutes. To remove excessive photoresist, the final device with DOMES was immersed in propylene glycol monomethyl ether acetate (PGMEA, MicroChem, Newton, MA) for a few minutes, followed by IPA rinse. Since such microstructure was printed right above the through hole, the trapped resin was readily dissolved using PGMEA, giving rise to a shorter development time compared to those microstructures created on intact films.

Soft lithography was utilized to fabricate top PDMS layer. Basically, any fabrication method that satisfies the resolution requirements can be used for creating master moulds, including photolithography,¹⁰ 3D printing,⁵⁸ micromachining,⁵⁹ and others.^{60,61} Afterwards, PDMS cover was attached directly onto PET substrate manually without additional treatments.

As the bonding was performed manually, cares should be taken during the whole process. Moreover, both surfaces should be cleaned thoroughly before contacting each other so as to give a stronger molecular contact between them *via* van der Waals forces.³⁵ Despite the fact that such reversible bonding did not provide comparable sealing strength compared to other methods such as plasma bonding, it allowed for the realization of the concept of stick-and-play. Moreover, microchannels became available for direct cleaning upon the separation of the cover and the substrate, thus making the reuse possible. Lastly, we attached the device to a ring-shaped piezo (APC International, Mackeyville, PA) with the help of a transparent double-sided tape. The piezo had a resonant frequency of 99.0 kHz with a 40 mm external diameter and a 20 mm diameter hole in the center, through which we were able to observe the pumping effects under microscope.

In contrast to the micromixer reported in our previous work,³⁷ the DOMES proposed in this paper had a rectangular profile with a curved contour in its top and tail (Fig. 1b), which allowed incoming flows to pass by smoothly without exerting extra pressure to the microstructures. Moreover, the

pores for creating air–liquid interfaces only existed on one side of the microstructures (Fig. 1c). Since the microstreaming was only expected to occur in the vicinity of these interfaces, the hypothesis is that rectified flows can be generated upon the activation of acoustic waves. Moreover, to obtain a stable adhesion between the DOMES and the PET film, an expanded base with larger contact area was applied in the design. Fig. 1d illustrated schematically the 3D model for a half DOMES, which was created above a through hole. This clearly indicates how the DOMES was deployed. Finally, a scheme illustrated the whole setup for the final device was shown in Fig. 1e.

2.2 DOMES and associated acoustic performance

Since through holes were pre-cut in the PET substrates, and DOMES were printed right above these holes, the trapped air–liquid interfaces were found to be very stable, thus maintaining stable acoustic microstreaming upon acoustic actuation. This benefit can be attributed to the fact that the bottom sides of these interfaces were always facing ambient air.

In this study, two different designs of DOMES were adopted, and both had the same profile except for the pore size. Basically, the DOMES had a cuboid base (300 μm in length, 270 μm in width, and 2 μm in thickness) and a curved shell (265 μm in length, 230 μm in width, and 25 μm in height) with pores in its front wall. Note that the total area of the pores in two designs was kept the same. The first design had 9 square pores with length of 15 μm , and the second design had 5 square pores with length of 20 μm .

For instance, DOMES with 20 μm square pore was printed above a through hole, and the corresponding scanning electron microscope (SEM) image taken by the SEM system (Hitachi S-3000 N-VP-SEM, Japan) is shown in Fig. 2a. It illustrated that the adaptive slicing and hatching parameters used successfully led to a smooth surface with a curved tail. In

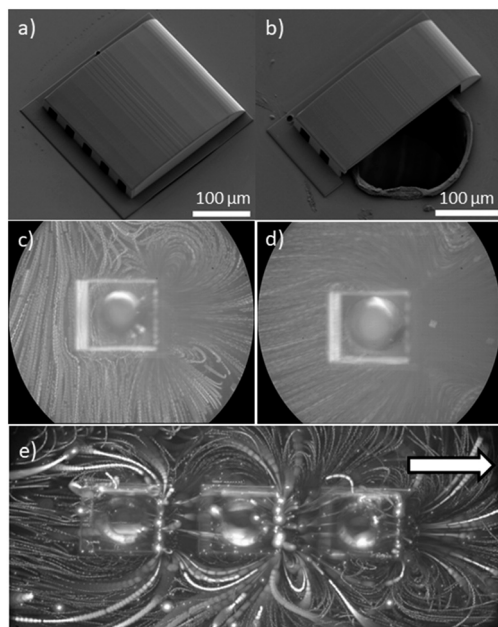


Fig. 2 SEM images of the DOMES as well as associated acoustic performances. a) SEM image of the DOMES with 20 μm pore; b) SEM image illustrating how a half DOMES was created above a through hole; c) rectified flows generated by the DOMES with 15 μm pores; d) stronger rectified flows generated by the DOMES with 20 μm pores; e) a net flow (indicated by the arrow) was created using three DOMES. All the images for microstreaming were obtained by superimposing 24 frames in a 1 second video clip.

addition, we also created a half DOMES, and its SEM image is shown in Fig. 2b. Despite the fact that protruding edges formed during hole preparation may apply undesired obstructions in TPP fabrication, the half microstructure remained intact without any deformation or undesired partition.

To further validate the value of the through hole for maintaining acoustic performance, we created one DOMES with 20 μm pores above the hole, and another identical one on intact PET film. Afterwards, small droplets of deionized (DI) water with 2.0 μm diameter fluorescent microparticles (Fluoro-Max dyed polystyrene microspheres, Thermo Fisher Scientific, Waltham, MA) were added to both films to visualize the corresponding pumping performance. It should be noted that both tests were carried out on free surface films without any top layer. Thereafter, they were attached to a ring-shaped piezo (APC International, Mackeyville, PA), which was actuated by a function generator (DG1022U; Rigol Technologies Inc., Beijing, China), associated with a voltage amplifier (Tegam 2350, Tegam Inc., Madison, OH). It is worth noting that by simplifying the air-liquid interfaces into a flat rectangular shaped membrane and neglecting the influence of other membranes in the array, we can find the theoretical resonant frequency of the interfaces to be around 140 kHz.⁶² This frequency was used as a guideline for us to determine the frequency sweeping range in the experiment. Indeed, upon sweeping the frequency from 100 Hz to 150 kHz at 5 Vpp, we found that the DOMES exhibited strongest microstreaming at 32.6 kHz with the aid of a fluorescence illuminator (X-cite 120,

Lumen Dynamics, Ontario, Canada), an inverted microscope system (Nikon Eclipse Ti-S, Nikon Instruments Inc.), and a high-speed camera (Phantom Miro M310, Vision Research Inc., USA). As a result, we used 32.6 kHz as the driving frequency hereafter. In addition, the air trapped in the microstructures on intact PET film disappeared in less than 1 minute, while the other one remained effective for more than 30 minutes (total experimental time).

Furthermore, by comparing the acoustic performance of the DOMES printed above through holes (Fig. 2c and d), we also observed that larger pore led to stronger acoustic effect. This can be attributed to more energy dissipated along with increasing interface displacement.⁶³ It is worth mentioning that the phenomena were characterized at the height where DOMES were (the height of DOMES was much smaller compared to that of the entire liquid domain, *i.e.* the liquid droplet on the surface), as the microstreaming became weaker upon increasing the height of focal plane (away from the substrate). Notwithstanding, both DOMES indicated the pumping ability to generate rectified flows pointing from their tails to front walls. Moreover, two vortices were observed near the corners of DOMES on the pumping side. In addition, micropump based on multiple DOMES was also demonstrated. Three identical DOMES were deployed in a line, and each of them had a through hole cut beneath in advance. After the piezoelectric transducer was activated, a strong microstreaming occurred near the vicinity of the microstructures. Hereby, a net flow (towards right in Fig. 2e) was generated, and the microparticles suspended in the liquid were pushed consecutively.

3. Theory and simulations

3.1 Theoretical background

Besides the experimental results obtained above using free surface PET devices, computational studies pertinent to the proposed acoustofluidic micropump were also conducted to gain in-depth understanding of the physical mechanisms behind these phenomena. Generally speaking, acoustofluidic manipulation stems from two hydrodynamic properties that are commonly ignored in conventional cases, the non-linearity of the well-known Navier-Stokes equation and the compressibility of fluids.⁶⁴ Moreover, to achieve such ability, two phenomena are of the utmost importance. The first one is the microstreaming, where an extra steady component of the velocity field in the bulk of liquids is induced by acoustic energy.⁶⁵ The second phenomenon is the secondary radiation force (*i.e.*, Bjerknes force), which accounts for the movement of suspended objects such as microparticles and cells together with Stokes drag force.⁶⁶

To simulate and characterize the microstreaming induced by acoustic energy, two methods can be applied: simulation based on directly solving the nonlinear Navier-Stokes equation, or based on the separation of time scales.^{64,67} The latter one solves the thermoacoustic equations first to first order, associated with the impact of thermoviscous boundary layer near walls. Afterwards, the results of first-order fields could be applied to solve the time-averaged second-order equations,

determining the final forces acting on the objects suspended.⁶⁷ Specifically, thermoacoustic fields can be described using four scalar parameters (density ρ , pressure p , temperature T , and entropy s) and the velocity vector field \mathbf{v} . Moreover, the changes of ρ and s can be determined by the following two equations,

$$d\rho = \gamma\kappa\rho dp - \alpha\rho dT, \quad (1)$$

$$ds = \frac{C_p}{T} dT - \frac{\alpha}{\rho} dp, \quad (2)$$

where C_p , γ , κ , and α denote the specific heat capacity, the specific heat capacity ratio, the isentropic compressibility, and the isobaric thermal expansion coefficient, respectively.

In addition, given the fact that solving the governing differential equations analytically is only achievable in several ideal scenarios, approximation methods such as perturbation theory are of the great value in conducting simulations. Hereby, we applied this theory. Accordingly, parameters T , p , ρ , and velocity \mathbf{v} can be represented as follows:

$$T = T_0 + T_1 + T_2, \quad (3)$$

$$p = p_0 + p_1 + p_2, \quad (4)$$

$$\rho = \rho_0 + \rho_1 + \rho_2, \quad (5)$$

$$\mathbf{v} = \mathbf{0} + \mathbf{v}_1 + \mathbf{v}_2. \quad (6)$$

No-slip boundary conditions were applied to all the walls with constant temperature ($T = T_0$), and velocity ($\mathbf{v} = \mathbf{0}$). Furthermore, a harmonic time-dependent velocity component should be added to the oscillating interfaces. In our case,

$$\mathbf{n} \cdot \mathbf{v}_1 = v e^{-i\omega t} \quad (7)$$

was applied to the air-liquid interfaces formed in DOMES. Note that \mathbf{n} is the normal vector pointing out of the interfaces, and v , ω , and t represent the velocity amplitude, the angular frequency, and the time, respectively.

To solve the first order acoustic field, here we used the Thermoviscous Acoustics, Frequency Domain interface in the Acoustic Module of COMSOL Multiphysics. It was also worth mentioning that the thermodynamic heat transfer equation, the kinematic continuity equation, and the Navier-Stokes equation now become:⁶⁷

$$\partial_t T_1 = D_{th} \nabla^2 T_1 + \frac{\alpha T_0}{\rho_0 C_p} \partial_t p_1, \quad (8)$$

$$\partial_t p_1 = \frac{1}{\gamma\kappa} [\alpha \partial_t T_1 - \nabla \cdot \mathbf{v}_1], \quad (9)$$

$$\rho_0 \partial_t \mathbf{v}_1 = -\nabla p_1 + \eta \nabla^2 \mathbf{v}_1 + \beta \eta \nabla (\nabla \cdot \mathbf{v}_1), \quad (10)$$

where D_{th} , η , and β represent the thermal diffusivity, the dynamic viscosity, and the viscosity ratio of fluids, respectively. Afterwards, the second order time averaged microstreaming

can be solved using the laminar flow interface based on the first order results. Thereby, the continuity equation and Navier-Stokes equation have been transformed to:

$$\rho_0 \nabla \cdot \langle \mathbf{v}_2 \rangle = -\nabla \cdot \langle \rho_1 \mathbf{v}_1 \rangle, \quad (11)$$

$$\begin{aligned} \eta \nabla^2 \langle \mathbf{v}_2 \rangle + \beta \eta \nabla (\nabla \cdot \mathbf{v}_2) - \langle \nabla p_2 \rangle \\ = \langle \rho_1 \partial_t \mathbf{v}_1 \rangle + \rho_0 \langle (\mathbf{v}_1 \cdot \nabla) \mathbf{v}_1 \rangle. \end{aligned} \quad (12)$$

As a result, the first, second order acoustic fields can be calculated, which were further applied for determining the forces acting on the objects suspended. The secondary radiation force F_{rad} , and Stokes drag force F_{drag} can be calculated using the following equations,⁶⁷⁻⁶⁹

$$F_{rad} = -\pi a^3 \left[\frac{2\kappa_0}{3} \text{Re}[f_1^* p_1^* \nabla p_1] - \rho_0 \text{Re}[f_2^* \mathbf{v}_1^* \cdot \nabla \mathbf{v}_1] \right], \quad (13)$$

$$F_{drag} = 6\pi\eta a (\langle \mathbf{v}_2 \rangle - \mathbf{u}), \quad (14)$$

where a , κ_0 , f_1 , f_2 , \mathbf{u} , and the asterisk symbol represent the radius of the spherical particle suspended, the compressibility of the fluid, the two pre-factors, the velocity of the particle, and the complex conjugation, respectively. Here, we applied the particle tracing for fluid flow interface to simulate the trajectories of the microparticles.

3.2 Simulation results

To simplify the geometry and avoid the heavy workload of calculation using 3D model, in this paper, two-dimensional (2D) model (Fig. 3a) was adopted for the simulation of DOMES-based micropump. Basically, the microchannel and the DOMES were represented by a block with the length and width of 600 μm , and a square polygon (width of 220 μm) with several segments, respectively. It is worth noting that the interfaces were marked in red with a length of 20 μm . The horizontal lines in the external block denoted the walls of the microchannel, and their mechanical conditions were set to be no-slip. Similarly, the walls on the DOMES except the interfaces were set to be no-slip. Thereafter, a harmonic time-dependent velocity component was added to the interfaces, associated with an amplitude of 50 nm, and a frequency of 32.6 kHz. It should also be noted that since the microchannel was far longer than 600 μm , periodic conditions should be applied to the vertical lines (orange) of the external block. Moreover, the liquid used in the fluid domain (area between the block and the DOMES) was set to be regular water, and the initial flow velocity was set to be 0.

As shown in Fig. 3b, the microstreaming plot indicated that the result had a great agreement with the experimental results, that was, a net flow was generated by the DOMES. The water in the fluid domain first bypassed the DOMES, and then converged in the center, giving rise to a continuous flow. Similar to the experimental results, two vortices were generated near the corners of DOMES in the pumping side,

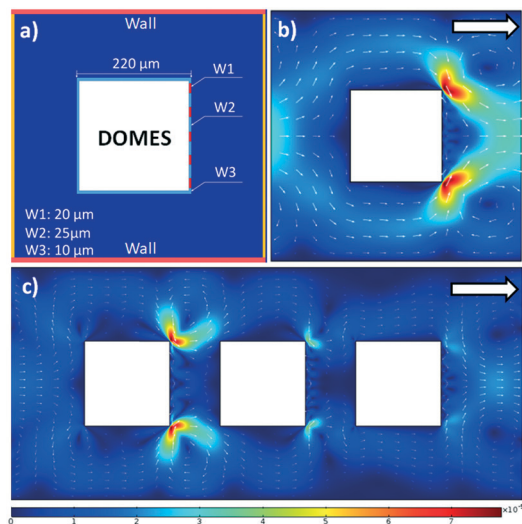


Fig. 3 The geometry and simulation results for DOMES-based micro-pump. a) The scheme illustrating the geometry and dimensions used in the simulation. W1, W2, and W3 denoted the widths of interfaces (red lines), walls between interfaces, and side walls, respectively. The horizontal lines (pink) represented the walls of the microchannel, while the vertical lines (orange) were set to periodic conditions; b) velocity field illustrating the acoustofluidic pumping effect due to single DOMES (color legend not shown); c) velocity field illustrating acoustofluidic pumping effect due to multiple DOMES. The arrows in the micro-streaming velocity plots indicated the flow directions, and the unit of the color legend is m s^{-1} .

where the flows and objects suspended can be trapped. Additionally, we also simulated the case, in which multiple DOMES were utilized to generate pumping effects (Fig. 3c). Specifically, three DOMES were adopted and deployed in a line; the gap between them was $350 \mu\text{m}$, identical to that in the experiments. Here, the harmonic time-dependent velocity component was added to 15 interfaces and all the other walls were set to be no-slip. After the calculation, we found that multiple DOMES also had the capability to generate rectified flow along the microchannel, and vortices still existed near the corners of DOMES.

However, it was worth mentioning that the flows in the regions between the DOMES had an opposite flow direction, which was contradictory to the experimental findings. This can be attributed to the fact that the fluids were capable of flowing above the DOMES in a 3D case, while in a 2D case, the flows were blocked by the front microstructure and had to turn back. Notwithstanding this limitation, the simulated results manifested that the DOMES was able to achieve pumping effects, and had shown the capabilities in assisting future designs. Furthermore, the particle tracing for fluid flow interface of COMSOL Multiphysics was applied for tracking the trajectories of the particles suspended in the fluid domain. The involving particles were set to be $2.0 \mu\text{m}$ diameter polystyrene beads, which had the same properties of the fluorescent particles used in the aforementioned experiments. A video showing the final results can be found in the ESI† (Video S1).

4. Experimental results and discussion

4.1 Pumping performance

As aforementioned, stick-and-play method provides several advantages in those cases, where strong bonding is not required. Given that acoustic micropumps usually do not generate high pressure, in this paper, PDMS cover with microchannel created by standard soft lithography was reversibly bonded to PET film manually. The PDMS cover contained a straight microchannel (length of 12 mm and width of $600 \mu\text{m}$) as well as two holes punched in advance using a biopsy punch (Ted Pella, Redding, CA), working as the inlet and outlet. Three DOMES with $20 \mu\text{m}$ pores and a center-to-center distance of $350 \mu\text{m}$ were incorporated in the microchannel. The final as-prepared lab-on-a-foil device was then attached to the ring-shaped piezo and activated at 32.6 kHz.

Note that these microstructures were deployed preferably close to the inlet in the center of the microchannel, by which DI water suspended with $2.0 \mu\text{m}$ diameter fluorescent microparticles could initially pass the microstructures *via* capillary action, forming the interfaces on the pores. Hereafter, micropump was activated to generate continuous flow inside the microchannel. However, after the flow reached the outlet, the micropump was deactivated to set the equilibrium state for the fluid. This step was inevitable since the pressure heads between the inlet and outlet could negatively affect the actual flow rate generated by DOMES.

After the equilibrium state was obtained, the micropump was activated again, and its initial performance was adopted for the quantification of the flow rates due to possible influence from different pressure heads between inlet and outlet after pumping for a while. Specifically, the average flow rate was calculated from the average velocities of the microparticles observed in videos, such as video S2 in the ESI.† Since our channel has a rectangular cross-sectional shape with an aspect ratio of 1 : 6, the velocity profile will deviate from parabolic shape in the width direction mimicking a Hele-Shaw flow condition.^{64,70} The average flow rate was estimated from the microparticle velocities observed in videos with the assumption of parabolic velocity profile along the height and plug-like flow along the width of the channel. We investigated the impact of input voltage on the pumping performance (Fig. 4). It was found that as the voltage increased, the flow rate generated by the micropump increased accordingly. When the input voltage was 1 Vpp, the flow rate was only 90 nL min^{-1} , yet it increased dramatically to 420 nL min^{-1} when the voltage was 4 Vpp. Despite having a relatively low flow rate when compared to other acoustic micropumps such as sharp edge based devices,^{71,72} the proposed micropump did not suffer from bubble instability and undesired bubble-trapping in the corners. Moreover, DOMES-based micropump possessed a high resolution in terms of flow rate control. That said, it was capable of tuning the flow rates in a fine range upon adjusting the input voltage carefully.

4.2 Microparticle and single-cell trapping

Similar to conventional microfluidic devices, to a large extent, single-cell traps based on encaging designs developed hitherto were generally fabricated using 2D designs.^{43,46} Although these traps were capable of trapping an individual cell, the involving cages were usually large. Therefore, only large cells (more than 10 μm in diameter) can be entrapped. Additionally, these devices were only able to trap cells in a fixed height due to the limitations from 2D designs. Hence, spatial impacts from vertical axis were commonly ignored.

In this paper, advantages of TPP such as high resolution and capabilities in 3D printing were exploited to create single-cell trapping microstructures, which were finally incorporated for creating self-pumped lab-on-a-foil single-cell trapping devices. Specifically, the single-cell trap used was a cylindrical open cage with tapering inlet and straight outlet (Fig. 5a), which were designed to trap cells and discharge fluids, respectively. The tapering inlet had a maximal diameter of 8 μm , a minimal diameter of 4 μm and a depth of 5 μm . Moreover, the straight outlet microchannel had a diameter of 4 μm . Herein, it was expected that single microparticle or cell with size around 5 μm could be trapped in the cage. To support the cage, another cylindrical microstructure was created underneath, by which the height of the region where the trapping carried out can be adjusted.

Prior to the use of actual cells to validate the functionality of such trapping approach, 4.8 μm diameter fluorescent microparticles (Fluoro-Max dyed polystyrene microspheres, Thermo Fisher Scientific, Waltham, MA) were utilized for initial investigation. That was, stick-and-play microfluidic device identical to the one described above was used in this case, yet a 3 by 3 array of traps were also built and incorporated in the center of the microchannel after the DOMES region. After the fluid with microparticles was pumped through upon the activation of the micropump, we found that despite microparticle trapping happening in the microstructure, a number of microparticles were also attached to the base (Fig. 5b). This can be attributed to the fact that a thin layer of unpolymerized photoresist still remained on the exterior surfaces of the polymerized microstructure even after a thorough development.⁵⁶ As a result, the surface could be sticky and readily for microparticle attachment.

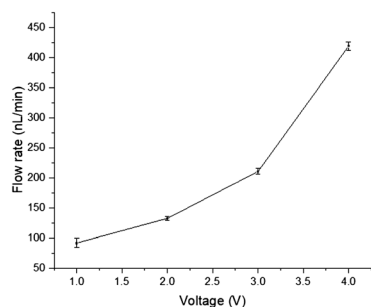


Fig. 4 Plot of pumping flow rate versus voltage illustrating the fact that flow rate increased along with the increase of input voltage.

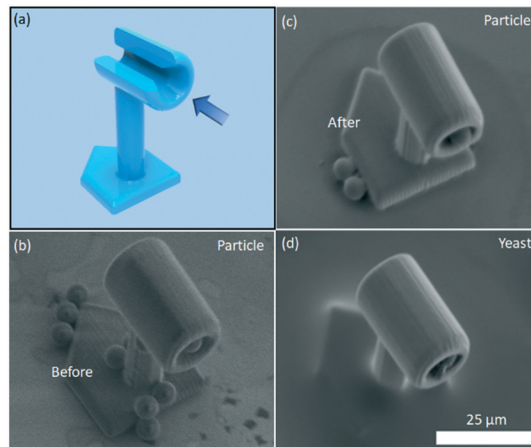


Fig. 5 Single-cell trap used in the self-pumped lab-on-a-foil device. a) A 3D model of the cell trap illustrating its working mechanism. The blue arrow indicates the flow direction; b) microparticle trapping using the cell trap without post polymerization. A number of microparticles were found to be attached to the microstructure; c) microparticle trapping using the cell trap with post polymerization. Only a few microparticles were found to be attached to the microstructure; d) single-cell trapping on the foil using yeasts as a test type.

Given this concern, a post polymerization using an UV lamp would be preferable. Herein, BlueWave® 200 Light-Curing Spot Lamp (Dymax Corporation, Torrington, CT) was used to conduct 5 minute polymerization on the final trapping microstructures. As shown in the Fig. 5c, the microstructure became less sticky, only a few microparticles were attached to the surface. Nevertheless, the result also demonstrated that the proposed microstructure was capable of trapping a single microparticle in the cage.

To test the feasibility of our single-cell trap using live cells, we used the budding yeast *Saccharomyces cerevisiae*. Yeast offers several advantages: size is amenable for the trap ($\sim 5 \mu\text{m}$), and compared to the microparticles, yeast are less sticky which enable us to trap them inside the cage (Fig. 5d). Importantly, we did not find yeast attached to the base or other areas. Note that the budding event was also observed in this SEM image.

Yeast is a powerful model system for basic eukaryotic biology study due to its genetic tractability, ability to perform high-throughput experiments and the conservation of many signaling pathways to humans. Yeast has been used as a pioneer model system in aging research,⁷³ cellular signaling pathways,⁷⁴ and even to understand basic biology of highly complex neurological diseases.^{75,76} Therefore, our microfluidics design can provide an important tool to facilitate high-throughput studies needed to circumvent major roadblocks in the field of aging, which can speed and enrich for large quantities of the replicative aged cells for RNA sequencing and other type of studies.

5. Conclusions

To sum up, we developed a novel stick-and-play acousto-fluidic micropump on the foil based on the microstructures

termed DOMES. Compared to regular acoustic bubbles or sharp edge based micropumps, our devices did not suffer from problems such as bubble instability, gas dissolution and undesired bubble-trapping in the corners, which could affect or even cease the pumping performance. More specifically, the DOMES were created above the through holes pre-cut in flexible PET films using TPP, and the pores designed on these microstructures were able to form air-liquid interfaces upon the arrival of fluids. As the pores were deployed asymmetrically, rectified flows can be generated after acoustic energy was activated. It was worth mentioning that larger pores were found to be able to generate stronger microstreaming, further leading to faster flows. We also capitalized on multiple DOMES to create better pumping performance, and the results indicated a good agreement with simulation results.

In addition, PDMS cover was used to form enclosed microchannels in a stick-and-play mode for characterizing the pumping performance. Herein, the final device could be disassembled and cleaned for reuse. A maximum flow rate of 420 nL min⁻¹ was obtained using three DOMES at 4 Vpp. Although such performance was not competitive to those obtained using other methods such as sharp edges, it did not suffer from problems such as bubble instability. Moreover, conventional microfluidic devices were built on rigid substrates such as glass slides, hence they lacked the capabilities of bending. Finally, we incorporated the proposed micropump with 3D cell traps for creating a self-pumped single-cell trapping device. That was, a simple 3D encaging trap was created using TPP, and the cumulative results indicated that it was capable of trapping single microparticle or yeast, as a test type. Compared to conventional single-cell cages with 2D designs, spatial control in the vertical axis could be considered in such 3D design, thus offering new possibilities in the future studies.

Admittedly, a few shortcomings to this proof-of-concept device still existed. For instance, compared to LCAT-based micropumps, multiple pumping components cannot be created simply through soft lithography, yet they should be created one by one *via* TPP, leading to a relatively long fabrication time. Moreover, TPP technology is currently still not a widely accessible method, thereby the applicability of this method is temporarily limited. In the future work, non-planar piezoelectric transducers such as film or 3D printed piezoelectric transducers could be used to further exploit the flexibility of such proposed micropump. We believe with such feature, acoustofluidic micropumps could become a promising tool with tremendous advantages and make invaluable contributions to various applications.

Conflicts of interest

The authors declare no conflict of interest.

Acknowledgements

This work was supported by an Early Career Faculty grant (80NSSC17K0522) from NASA's Space Technology Research

Grants Program. Yuan Gao thanks the financial support from Sigma Xi Grants-in-Aid of Research program (G2018100198272403).

Notes and references

- 1 A. Manz, N. Graber and H. á. Widmer, *Sens. Actuators, B*, 1990, **1**, 244–248.
- 2 M. Wu, P. H. Huang, R. Zhang, Z. Mao, C. Chen, G. Kemeny, P. Li, A. V. Lee, R. Gyanchandani and A. J. Armstrong, *Small*, 2018, **14**, 1801131.
- 3 D. B. Weibel and G. M. Whitesides, *Curr. Opin. Chem. Biol.*, 2006, **10**, 584–591.
- 4 A. Ainla, E. T. Jansson, N. Stepanyants, O. Orwar and A. Jesorka, *Anal. Chem.*, 2010, **82**, 4529–4536.
- 5 Y. Lin, D. Gritsenko, S. Feng, Y. C. Teh, X. Lu and J. Xu, *Biosens. Bioelectron.*, 2016, **83**, 256–266.
- 6 A. De Vellis, D. Gritsenko, Y. Lin, Z. Wu, X. Zhang, Y. Pan, W. Xue and J. Xu, *Sens. Actuators, B*, 2017, **243**, 298–302.
- 7 S. Zhao, W. He, Z. Ma, P. Liu, P.-H. Huang, H. Bachman, L. Wang, S. Yang, Z. Tian, Z. Wang, Y. Gu, Z. Xie and T. J. Huang, *Lab Chip*, 2019, **19**(6), 941–947.
- 8 A. R. Tovar and A. P. Lee, *Lab Chip*, 2009, **9**, 41–43.
- 9 P.-H. Huang, N. Nama, Z. Mao, P. Li, J. Rufo, Y. Chen, Y. Xie, C.-H. Wei, L. Wang and T. J. Huang, *Lab Chip*, 2014, **14**, 4319–4323.
- 10 Y. Lin, C. Gao, D. Gritsenko, R. Zhou and J. Xu, *Microfluid. Nanofluid.*, 2018, **22**, 97.
- 11 L. Dong, M. Cornaglia, T. Lehnert and M. A. Gijs, *Lab Chip*, 2016, **16**, 574–585.
- 12 S. Jang, B. Lee, H.-H. Jeong, S. H. Jin, S. Jang, S. G. Kim, G. Y. Jung and C.-S. Lee, *Lab Chip*, 2016, **16**, 1909–1916.
- 13 D. Patra, S. Sengupta, W. Duan, H. Zhang, R. Pavlick and A. Sen, *Nanoscale*, 2013, **5**, 1273–1283.
- 14 M. V. Patel, I. A. Nanayakkara, M. G. Simon and A. P. Lee, *Lab Chip*, 2014, **14**, 3860–3872.
- 15 F. Amirouche, Y. Zhou and T. Johnson, *Microsyst. Technol.*, 2009, **15**, 647–666.
- 16 X. Wang, C. Cheng, S. Wang and S. Liu, *Microfluid. Nanofluid.*, 2009, **6**, 145–162.
- 17 Y.-N. Wang and L.-M. Fu, *Microelectron. Eng.*, 2018, **195**, 121–138.
- 18 M. V. Patel, A. R. Tovar and A. P. Lee, *Lab Chip*, 2012, **12**, 139–145.
- 19 T. Ma, S. Sun, B. Li and J. Chu, *Sens. Actuators, A*, 2019, **292**, 90–96.
- 20 X. Y. Wang, Y. T. Ma, G. Y. Yan, D. Huang and Z. H. Feng, *Sens. Actuators, A*, 2014, **218**, 94–104.
- 21 J. Chen, D. Huang and Z. H. Feng, *Smart Mater. Struct.*, 2015, **24**, 105009.
- 22 J. Fong, Z. Xiao and K. Takahata, *Lab Chip*, 2015, **15**, 1050–1058.
- 23 A. V. Lemoff and A. P. Lee, *Sens. Actuators, B*, 2000, **63**, 178–185.
- 24 M. Russel, S. Hasnain, P. Selvaganapathy and C. Ching, *Microfluid. Nanofluid.*, 2016, **20**, 112.

- 25 S.-C. Lin, J.-C. Lu, Y.-L. Sung, C.-T. Lin and Y.-C. Tung, *Lab Chip*, 2013, **13**, 3082–3089.
- 26 W.-F. Fang and A. P. Lee, *Microfluid. Nanofluid.*, 2015, **18**, 1265–1275.
- 27 A. Oskooei and A. Günther, *Lab Chip*, 2015, **15**, 2842–2853.
- 28 A. Ozcelik, J. Rufo, F. Guo, Y. Gu, P. Li, J. Lata and T. J. Huang, *Nat. Methods*, 2018, **1**.
- 29 S. Girardo, M. Cecchini, F. Beltram, R. Cingolani and D. Pisignano, *Lab Chip*, 2008, **8**, 1557–1563.
- 30 L. Schmid, A. Wixforth, D. A. Weitz and T. Franke, *Microfluid. Nanofluid.*, 2012, **12**, 229–235.
- 31 R. W. Rambach, K. Linder, M. Heymann and T. Franke, *Lab Chip*, 2017, **17**, 3422–3430.
- 32 J. Chen, X. He, W. Wang, W. Xuan, J. Zhou, X. Wang, S. Dong, S. Garner, P. Cimo and J. Luo, *J. Mater. Chem. C*, 2014, **2**, 9109–9114.
- 33 H. Jin, J. Zhou, X. He, W. Wang, H. Guo, S. Dong, D. Wang, Y. Xu, J. Geng and J. Luo, *Sci. Rep.*, 2013, **3**, 2140.
- 34 A. R. Tovar, M. V. Patel and A. P. Lee, *Microfluid. Nanofluid.*, 2011, **10**, 1269–1278.
- 35 A. Wasay and D. Sameoto, *Lab Chip*, 2015, **15**, 2749–2753.
- 36 Y. Nakashoji, H. Tanaka, K. Tsukagoshi and M. Hashimoto, *Electrophoresis*, 2017, **38**, 296–304.
- 37 Y. Lin, C. Gao, Y. Gao, M. Wu, A. A. Yazdi and J. Xu, *Sens. Actuators, B*, 2019, **287**, 312–319.
- 38 M. Focke, D. Kosse, C. Müller, H. Reinecke, R. Zengerle and F. von Stetten, *Lab Chip*, 2010, **10**, 1365–1386.
- 39 G. S. Fiorini and D. T. Chiu, *BioTechniques*, 2005, **38**, 429–446.
- 40 M. Focke, F. Stumpf, B. Faltin, P. Reith, D. Bamarni, S. Wadle, C. Müller, H. Reinecke, J. Schrenzel and P. Francois, *Lab Chip*, 2010, **10**, 2519–2526.
- 41 Y. Kuang, I. Biran and D. R. Walt, *Anal. Chem.*, 2004, **76**, 6282–6286.
- 42 S. Skylaki, O. Hilsenbeck and T. Schroeder, *Nat. Biotechnol.*, 2016, **34**, 1137.
- 43 D. Di Carlo, N. Aghdam and L. P. Lee, *Anal. Chem.*, 2006, **78**, 4925–4930.
- 44 D. Ahmed, A. Ozcelik, N. Bojanala, N. Nama, A. Upadhyay, Y. Chen, W. Hanna-Rose and T. J. Huang, *Nat. Commun.*, 2016, **7**, 11085.
- 45 D. A. Lawson, N. R. Bhakta, K. Kessenbrock, K. D. Prummel, Y. Yu, K. Takai, A. Zhou, H. Eyob, S. Balakrishnan and C.-Y. Wang, *Nature*, 2015, **526**, 131.
- 46 A. R. Wheeler, W. R. Thronset, R. J. Whelan, A. M. Leach, R. N. Zare, Y. H. Liao, K. Farrell, I. D. Manger and A. Daridon, *Anal. Chem.*, 2003, **75**, 3581–3586.
- 47 S. Stavrakis, G. Holzner and J. Choo, *Curr. Opin. Biotechnol.*, 2019, **55**, 36–43.
- 48 E. Brouzes, M. Medkova, N. Savenelli, D. Marran, M. Twardowski, J. B. Hutchison, J. M. Rothberg, D. R. Link, N. Perrimon and M. L. Samuels, *Proc. Natl. Acad. Sci. U. S. A.*, 2009, **106**, 14195–14200.
- 49 L. Mazutis, J. Gilbert, W. L. Ung, D. A. Weitz, A. D. Griffiths and J. A. Heyman, *Nat. Protoc.*, 2013, **8**, 870.
- 50 P. S. Hoppe, M. Schwarzfischer, D. Loeffler, K. D. Kokkaliaris, O. Hilsenbeck, N. Moritz, M. Ende, A. Filipczyk, A. Gambardella and N. Ahmed, *Nature*, 2016, **535**, 299.
- 51 S. J. Tan, L. Yobas, G. Y. H. Lee, C. N. Ong and C. T. Lim, *Biomed. Microdevices*, 2009, **11**, 883–892.
- 52 J. R. Rettig and A. Folch, *Anal. Chem.*, 2005, **77**, 5628–5634.
- 53 B. M. Taff and J. Voldman, *Anal. Chem.*, 2005, **77**, 7976–7983.
- 54 F. Arai, C. Ng, H. Maruyama, A. Ichikawa, H. El-Shimy and T. Fukuda, *Lab Chip*, 2005, **5**, 1399–1403.
- 55 B. Hammarström, M. Evander, H. Barbeau, M. Bruzelius, J. Larsson, T. Laurell and J. Nilsson, *Lab Chip*, 2010, **10**, 2251–2257.
- 56 Y. Lin and J. Xu, *Adv. Opt. Mater.*, 2018, **6**, 1701359.
- 57 Y. Lin, R. Zhou and J. Xu, *Adv. Opt. Mater.*, 2018, **5**, 1801126.
- 58 K.-i. Kamei, Y. Mashimo, Y. Koyama, C. Fockenber, M. Nakashima, M. Nakajima, J. Li and Y. Chen, *Biomed. Microdevices*, 2015, **17**, 36.
- 59 J. Park, J. Li and A. Han, *Biomed. Microdevices*, 2010, **12**, 345–351.
- 60 D. A. Bartholomeusz, R. W. Boutté and J. D. Andrade, *J. Microelectromech. Syst.*, 2005, **14**, 1364–1374.
- 61 S. Brittan, S. Z. Oener, K. Guo, H. Āboliņš, A. F. Koenderink and E. C. Garnett, *J. Mater. Chem. C*, 2017, **5**, 8301–8307.
- 62 C. Chindam, N. Nama, M. I. Lapsley, F. Costanzo and T. J. Huang, *J. Appl. Phys.*, 2013, **114**, 194503.
- 63 D. Gritsenko, Y. Lin, V. Hovorka, Z. Zhang, A. Ahmadianyazdi and J. Xu, *Phys. Fluids*, 2018, **30**, 082001.
- 64 H. Bruus, *Theoretical microfluidics*, Oxford university press Oxford, 2008.
- 65 A. Hashmi, G. Heiman, G. Yu, M. Lewis, H.-J. Kwon and J. Xu, *Microfluid. Nanofluid.*, 2013, **14**, 591–596.
- 66 Y. Chen, Z. Fang, B. Merritt, D. Strack, J. Xu and S. Lee, *Lab Chip*, 2016, **16**, 3024–3032.
- 67 P. B. Muller, R. Barnkob, M. J. H. Jensen and H. Bruus, *Lab Chip*, 2012, **12**, 4617–4627.
- 68 M. Settnes and H. Bruus, *Phys. Rev. E: Stat., Nonlinear, Soft Matter Phys.*, 2012, **85**, 016327.
- 69 J. T. Karlsen and H. Bruus, *Phys. Rev. E: Stat., Nonlinear, Soft Matter Phys.*, 2015, **92**, 043010.
- 70 P. Tabeling, *Introduction to microfluidics*, Oxford University Press on Demand, 2005.
- 71 N. Nama, P.-H. Huang, T. J. Huang and F. Costanzo, *Lab Chip*, 2014, **14**, 2824–2836.
- 72 P.-H. Huang, Y. Xie, D. Ahmed, J. Rufo, N. Nama, Y. Chen, C. Y. Chan and T. J. Huang, *Lab Chip*, 2013, **13**, 3847–3852.
- 73 M. C. Jo, W. Liu, L. Gu, W. Dang and L. Qin, *Proc. Natl. Acad. Sci. U. S. A.*, 2015, **112**, 9364–9369.
- 74 G. Caraveo, P. K. Auluck, L. Whitesell, C. Y. Chung, V. Baru, E. V. Mosharov, X. Yan, M. Ben-Johny, M. Soste and P. Picotti, *Proc. Natl. Acad. Sci. U. S. A.*, 2014, **111**, E3544–E3552.
- 75 P. K. Auluck, G. Caraveo and S. Lindquist, *Annu. Rev. Cell Dev. Biol.*, 2010, **26**, 211–233.
- 76 V. Khurana and S. Lindquist, *Nat. Rev. Neurosci.*, 2010, **11**, 436.